Archaeological and Anthropological Sciences (2020) 12:162
https://doi.org/10.1007/s12520-020-01090-6

ORIGINAL PAPER

Bone diagenesis in archaeological and contemporary human remains: an investigation of bone 3D microstructure and minero-chemical assessment

Valentina Caruso[1,2] · Nicoletta Marinoni[1] · Valeria Diella[3] · Francesco Berna[4] · Marco Cantaluppi[1] · Lucia Mancini[5] · Luca Trombino[1] · Cristina Cattaneo[2] · Linda Pastero[6] · Alessandro Pavese[6]

Received: 25 February 2020 / Accepted: 21 May 2020

Abstract

The major difficulty to study bone preservation is to define which diagenetic parameters need to be taken into account when any information on environmental conditions is missing. Through this research, we contribute towards understanding the complex interplay of factors that affects human bones during diagenetic process. The work focuses on how organic and mineral components influence each other and how they influence the resulting micro-structural assessment of human bone. The mineral and organic properties of 24 adult human long bones from archaeological to contemporary burials in Milan (Italy) were characterized through different analytical techniques, in relation to the preservation of their microstructure and porosity. The 3D microstructure of the bone tissue was carried out through the use of phase contrast synchrotron radiation computed micro-tomography (SR-μCT). The results show that when diagenesis proceeds, (i) the bone tissue is progressively attacked by microbes; (ii) the diagenetic porosity increases at the expense of vascular ones; (iii) the volumes, diameters, and interconnections of vascular canals are markedly reduced; (iii) the amount of organic and carbonate fraction decreases whereas bone crystallinity and mean crystal length increase; (iv) the Ca/P mole ratio in CHA crystals increases; (v) the anisotropy along *c*-axis in CHA crystals is lost, resulting in an increase of their domain size. Since the conservation of organic and mineral fractions is variable in relation to bone microstructure within the same period and site, the research points out the needs to perform a multi-analytical approach to characterize the bone diagenesis at different scales of observation.

Keywords Human bone diagenesis · Phase contrast synchrotron radiation computed micro-tomography (SR-μCT) · X-ray powder diffraction (XRPD) · Fourier transform infrared spectroscopy (FT-IR) · Electron microprobe analysis (EMPA)

Introduction

Human bone is a composite material made by carbonate-hydroxyapatite (CHA, 60–70 wt%), organic matter (mainly fibrous protein collagen, 20–30 wt%), and water (10 wt%), intimately associated with each other into a common building block (the mineralized collagen fibril) with a highly ordered structure (Weiner and Wagner 1998). The amount of organic

Electronic supplementary material The online version of this article (https://doi.org/10.1007/s12520-020-01090-6) contains supplementary material, which is available to authorized users.

✉ Valentina Caruso
caruso.valentina@libero.it

[1] Dipartimento di Scienze della Terra "Ardito Desio", Università degli Studi di Milano, Luigi Mangiagalli street n.34, 20133 Milan, Italy

[2] LABANOF, Laboratorio di Antropologia e Odontologia Forense, Sezione di Medicina Legale e delle Assicurazioni, Dipartimento di Scienze Biomediche per la Salute, Università degli Studi di Milano, Luigi Mangiagalli street n.37, 20133 Milan, Italy

[3] IGAG, Sezione di Milano, Consiglio Nazionale delle Ricerche, Sandro Botticelli street n.23, 20133 Milan, Italy

[4] Department of Archaeology, Simon Fraser University, 8888 University Drive, Burnaby, British Columbia, Canada

[5] Elettra-Sincrotrone Trieste S.C.p.A, Strada Statale 14 - km 163,5, Basovizza, 34149 Trieste, Italy

[6] Dipartimento di Scienze della Terra, Università degli Studi di Torino, Valperga Caluso Street n.35, 10123 Turin, Italy

Published online: 10 July 2020

and mineral phases, as well as their spatial arrangement (porosity, orientation, and microstructure), has a key role in defining the bone mechanical properties and in affecting its preservation after death (Reiche et al. 2002).

Before death, several extrinsic and intrinsic factors can influence the bone tissue properties (diet, age, mineral turnover, cell viability, health status, therapeutic modalities) (Boskey 2003), whereas after death, a bone undergoes many diagenetic changes, which depend on the time elapsed since death and on the burial settings (temperature, pH, water, soil chemistry, microbiological composition) (Wilson and Pollard 2002). In particular, post-mortem bones are primarily affected by a loss of structural collagen, whose proteins can be fully or partially replaced by inorganic precipitates (Collins et al. 2002). Owing to the collagen matrix decomposition, the carbonate-hydroxyapatite spontaneously loses some of the CO_3^{-2} groups, transforming into a more stable thermodynamically phase of CHA with a crystal habit very similar to that of hydroxyapatite (HA) (Berna et al. 2004).

Since the diagenetic process affects buried bones from macro- to nano-scale (Guarino et al. 2006), several levels of investigation are required to properly study recent and ancient buried specimens.

Many works are nowadays investigating the state of preservation of organic and mineral fractions and of microstructure as if they were independent of each other, without considering the possible correlations among them (Fernández-Jalvo et al. 2010; Reiche et al. 2010; Piga et al. 2013; Beasley et al. 2014; Lebon et al. 2014; France et al. 2014; White and Booth 2014; Booth and Madgwick 2016; Brönnimann et al. 2018; Caruso et al. 2018; Hollund et al. 2018; Tripp et al. 2018; Stathopoulou et al. 2013; Morales et al. 2017, and references therein). Other papers pay attention to the impact of the environment (for instance, water, pH, soil) on the bone diagenetic transformations (Abdel-Maksoud and Abdel-Hady 2011; Müller et al. 2011; Rogoz et al. 2012; Boaks et al. 2014; Monge et al. 2014; Dal Sasso et al. 2015; Keenan et al. 2015; Abdel-Maksoud and El-Sayed 2016; Huisman et al. 2017; Kendall et al. 2018; Kontopoulos et al. 2019; Margariti et al. 2019, and references therein). In particular, Nielsen-Marsh and Hedges (2000) point out that the local hydrology has a strong influence on the outcome of bone preservation and porosity appears to be the most effective single diagenetic parameter that determines and marks the degree of bone preservation in burial environment. Eventually, Kendall et al. (2018) claim that "the diagenetic mechanisms are found to work in conjuction with each other, altering the biogenic composition of skeletal material."

A wide number of analytical techniques, encompassing Fourier transform infrared spectroscopy (FT-IR), X-ray powder diffraction (XRPD), and optical microscopy, are being currently employed to characterize bone diagenesis in fossil, archaeological, and modern remains from a conventional histological, physical-chemical, and mineralogical point of view (Turner-Walker and Syversen 2002; Piga et al. 2009; Chadefaux et al. 2009a; Lebon et al. 2011, 2014, 2016; Hollund et al. 2013; Beasley et al. 2014; France et al. 2014; Schmahl et al. 2016; Dal Sasso et al. 2018; Marques et al. 2018; Kontopoulos et al. 2019; Ryanskaya et al. 2019). In the last years, several works stress the potential of the phase contrast synchrotron micro-computed tomography (SR-μCT) as a promising technique to reveal the complexity of 3D bone features (Cooper et al. 2003), as well as to investigate the degree of use-damage of ancient animal bone weapons (Bello et al. 2013; Bradfield 2013). In particular, in medical and bio-engineering field, SR-μCT was used to evaluate the bone stiffness and strength of trabeculae and cortical tissue (Palacio-Mancheno et al. 2014; Hollund et al. 2018; Marado et al. 2018; Morales et al. 2017), whereas in forensic anthropology and bioarchaeology, some works show the great potential of SR-μCT to provide an extraordinary level of details about the inner bone features and the related diagenetic alterations (Tripp et al. 2018; Amarante et al. 2019).

Many researches have focused on how bone diagenesis takes place in the early post-depositional period in fresh human bones and animal carcasses using different analytical techniques at laboratory scale and/or performing experiments at large-scale facilities (Peyrin et al. 2014; Maggiano et al. 2016; Le Garff et al. 2017a; Le Garff et al. 2017b; Soltan et al. 2019). However, studies combining the evaluation of the micro-structural bone tissue features and their physical-chemical and mineralogical properties, in regard to the organic and mineral fractions in human skeletons from archaeological to contemporary ages, are comparatively few.

An understanding of the diagenetic processes, in terms of preservation and decay over time, is crucial in bioarchaeology and physical anthropology, because bones can be likened to "windows" onto past lifeways, environments, and evolutionary histories (Müller et al. 2011). In case of unknown and highly fragmented remains, the suitability of a preserved bone tissue at histological scale allows one to perform several diagnoses, including species determination (human versus non-human) (Cattaneo et al. 2009), age of death (Kerley and Ubelaker 1978; Han et al. 2009), and disease (Assis et al. 2015). Chemical compositions of bones (and teeth) are a key for information about climate, environmental exposure, genetics, diets, health, dating, and migration (Evans et al. 2006; Brady et al. 2008; Castro et al. 2010 and the literature herein cited; Müller et al. 2011). All these data, synergically pieced together, allow assessment of the demographic trend, ethnic evolution, and health of past populations as well as of the funerary activities or other cultural practices (Ambrose and Krigbaum 2003; Szostek et al. 2011; Booth et al. 2016; Booth 2016).

In this light, this paper presents a multidisciplinary approach by combining traditional and unconventional analytical methods to fully characterize the post-mortem evolution of

twenty-four adult human bones from Late Roman to Contemporary burial settings, found in the Metropolitan City of Milan (Italy). In particular, the conservation of organic and mineral phases was investigated by FT-IR, XRPD, and electron microprobe in wavelength-dispersive mode (EMP-WDS). The micro-structural modifications of bones were analyzed by two-dimensional (2D) histological sections by conventional optical microscopy (OM) and scanning electron microscopy using backscattered electron images (SEM-BSE).

Starting from the previous studies by Nielsen-Marsh and Hedges (2000), we aim to move ahead. In particular, the characterization of the actual bone porosity has been performed by means of micro-tomography, which allows one to detect the actual 3D spatial distribution of pores within the bones. Owing to the high resolution required to detect from nano to micrometric bone micro-structural features, phase contrast SR-μCT appears to be the most appropriate technique to obtain a detailed characterization of the bone matrix, in terms of quantitative and morphometric analysis of its porosity attributed to (i) vascular canals and (ii) voids produced by tissue degradation (i.e., total porosity, pore size, tortuosity, orientation, and connectivity).

Therefore, the present research is a contribution to understanding the complex interplay of factors affecting human bones during the diagenetic process. In particular, the work focuses on how the organic and mineral components influence each other and how they affect the resulting microstructure of human bones.

Material and methods

Osteological materials

Twenty-four human bones were collected from four burial settings of the Metropolitan City of Milan (Italy). In particular, six bones (UC) belong to the Late Roman Age (from third to fifth century AD) and were discovered in Università Cattolica; twelve bones belong to the Modern Age, among which six are from Viale Sabotino (VS) (seventeenth century AD), and six from Ca' Granda (CG) (from sixteenth to the beginning of eighteenth century AD); six bones belong to the Contemporary Age (CM) (end of twentieth century AD) and come from Cimitero Maggiore. The Late Roman bones of Università Cattolica belong to individuals buried in ground, in single or multiple graves, inside a necropolis (Sannazaro 2001). The Modern bones of Viale Sabotino were sampled from a mass grave which hosted commingled skeletal remains of two hundred forty individuals died from a plague outbreak (Marsden and Pagani 2008). The Modern bones of Ca' Granda belong to an ossuary discovered inside the crypt of the Church of Santa Maria Annunciata, of the University of Milan. Since the fifteenth to eighteenth century AD, the present headquarter of the University of Milan was the greatest hospital of the city; therefore, the commingled skeletons that have been found probably belong to the patients who died during the hospitalization. The Contemporary bones from Cimitero Maggiore are unclaimed remains, buried in coffins in the cemetery, and exhumed after 15 years, when the skeletonization process was completed (Cattaneo et al. 2018). In accordance with the Police Mortuary Rules (DPR 09.10.90 n° 285, art. 43) and in virtue of an agreement between the municipality of Milan and the Department of Legal Medicine of the University of Milan, unclaimed human remains can be used for scientific research. The sex and age of the human bones were determined following standard anthropological methods (Beauthier et al. 2010; Brooks and Suchey 1990; Işcan et al. 1984; Rouge-Maillart et al. 2009) applied to the entire skeleton (see Appendix Table 2). In the case of commingled remains, information on sex was obtained only by metrical analysis of each bone.

Analytical methods

Optical microscopy

Thin cross sections were prepared for OM observations after Caruso et al. (2018) and analyzed with an Axio Scope.A1 light microscope, equipped with a True Chrome Hd II camera for image acquisition using IScapture® (version 3.6.7) software, with a resolution of 1920 × 1080. In OM, the histological destruction of bone (i.e., amount of unaltered bone versus amount of material affected by microbial attack and erosion) was estimated using the Oxford Histological Index (OHI) (Hedges et al. 1995). The degree of histological destruction is expressed in scores from 5 to 0. A score of 5 corresponds to less than 5% of bone tissue affected by deterioration (the microscopic histological features of the tissue appear identical to those of fresh bone), whereas a score of 0 indicates that less than 5% of the original bone features are preserved. For the sake of simplicity, the bone preservation level was determined by gathering histological destruction classes into three subclasses as follows: low = OHI 0–1; medium = OHI 2–3; high = OHI 4–5.

Scanning electron microscopy and electron microprobe analysis in wavelength-dispersive mode

Backscattered electron images on polished thin sections were performed using a Cambridge Stereoscan 360, with an acceleration current of 15 kV, a beam size of 100 nm, and a working distance of 11 mm. The 2D images were recorded with Oxford Link Pentafet software, with a resolution of 1024 × 730, where the pixel linear size is as large as 1.5 μm.

EMP-WDS was employed to carry out quantitative chemical analyses on thin sections, using a JEOL JXA-8200 EMP-

WDS, with an accelerating voltage of 15 kV, a beam current of 5 nA, and counting times of 30 s on peak and 10 s on background. Quantitative analysis of major (Ca, P) and minor (Fe, Al, Na, K, Si, Mn, Mg, Sr, Ba, S, Cl, F, La, and Ce) elements was performed. F, La, and Ce resulted under the detection limit.

Synchrotron X-ray micro-tomography

Phase contrast SR-μCT was used to obtain 3D microstructure reconstructions. Samples were "imaged" at the SYRMEP beamline of the Elettra synchrotron laboratory (Trieste, Italy), employing a filtered (1 mm Al + 1.5 mm Si) polychromatic X-ray beam delivered by a bending magnet source in transmission geometry. The sample-to-detector distance was set at 120 mm. The detector used was an air-cooled, 16 bit, sCMOS camera (Hamamatsu C11440-22C) with a 2048 × 2048 pixel chip coupled with a LSO:Tb scintillator screen (17 μm thick on the top of a 170 μm-thick LSO substrate) and a high numerical aperture optics. The effective pixel size of the detector was set at 2.1 × 2.1 μm^2, and the pixel array provided a total coverage of about 4.3 × 4.3 mm^2. From 1800 to 3000, projections were recorded rotating continuously each sample by 360° and using an exposure time/projection of 2 s.

Each set of collected raw images was processed by the STP (SYRMEP Tomo Project) software suite, developed in-house at Elettra (De Carlo et al. 2014; Brun et al. 2015), to perform image reconstruction by means of the filtered back-propagation algorithm. A filter for ring removal (Munch et al. 2009) was used to compensate for the so-called ring artifacts. From every set of slices, a volume of interest (VOI) was selected by Fiji (version 1.51e) (Schindelin et al. 2012); the porosity of total bone (TP) and vascular canals (CP) were addressed after Cooper et al. (2003). Moreover, diagenetic porosity (DP) was selected by digital subtraction of the vascular canal porosity from the total one. The 3D image analysis in order to extract quantitative parameters about the pore morphology and distribution was performed by the software library *Pore3D* which allowed calculation of the following: (i) volume fraction (V_v—volume of the vascular canal pore network/total volume) expressed as vol%; (ii) Euler characteristics (χ_V—an index associated with the connectedness of a 3D pore network and indicating the number of connections between voids per unit volume. χ_V is expressed in mm^{-3} and it is positive, when the number of isolated pores exceeds the number of multiple interconnections between pores, or negative, in the case of connected pore networks); iii) morphometric features of the vascular canal pore structure, such as size and aspect ratio. The skeletonization process, i.e., a thinning procedure for visualizing the "backbone" of the pore object, was carried out on the connected pores by applying the GVF algorithm (Brun and Dreossi 2010). The analysis of obtained skeletons allowed investigation of the actual connectivity of the pore network by computing the connectivity density parameter (Brun et al. 2010). The reconstructed volumes were visualized by 3D rendering procedures, using the commercial software VGStudio 3.1.2.

Fourier transform infrared spectroscopy

The samples were prepared according to Trueman et al. (2008) for FT-IR spectroscopy measurements. Bone powders were analyzed in transmission mode with a Thermo Scientific Nicolet iS5 transportable FT-IR spectrometer equipped with a transmission mode sampling chamber (model iD1). Absorption spectra in the 4000 to 400 cm^{-1} wavenumber range were collected recording 32 scans at a resolution of 4 cm^{-1}. Two samples for each bone population were measured in triplicate to account for sample variability and estimate instrumental error. Instrumental setup, spectra collection, and data analysis were carried out using Thermo-Nicolet Omnic (version 9) software. For each whole bone sample, the FT-IR absorption intensity bands of ν_1Amide I (1653 cm^{-1}), $\nu_3(PO_4^{-3})$ (1035 cm^{-1}), and $\nu_2(CO_3^{-2})$ (873 cm^{-1}) were measured (Trueman et al. 2004). The organic component (wt%) was estimated using the equation of Trueman et al. (2004). The degree of recrystallization of the bone mineral was determined by the infrared splitting factor (IRSF), calculated according to Winer and Bar-Yosef (1990). Since crystallinity is a measure of structural order within CHA that is directly related to the mean crystal length, the mean CHA crystallite length was indirectly estimated using the equation of Trueman et al. (2008).

X-ray powder diffraction

For the present study, the bone samples for bulk XRPD were pulverized and side loaded on a flat Al sample holder and measured by a Bragg-Brentano geometry PANalytical X'Pert Diffractometer, using CuKα radiation (1.5417 Å) (40 kV and 40 mA), and a X'Celerator detector, over the angular 2θ 5°–140°, with divergence slit of 1/2° and receiving slit of 0.1 mm as instrumental setting. The XRPD patterns were collected with a counting time of 100 s/step and with a 0.01° step and the collection time for each powder pattern was pursed for 120 min. The XRPD qualitative analysis was performed by PANalytical X'Pert HighScore software. Rietveld refinement (Young 1993) was performed on diffraction patterns using the GSAS-II program. Rietveld refinement was applied over the entire measured profile varying cell parameters, crystallite size, micro-strain, zero shift, and using a Chebyshev polynomial function with five terms to model background. Atomic thermal parameters, site occupancy, and atomic position were kept fixed at their values from literature during refinement (Cheary and Coelho 1992). The

hexagonal structure model of Sudarsan and Young (1969) was employed. The peak widths are *hkl* dependent and the plot of FWHM values of resolved reflections as a function of 2θ well indicates that structural imperfections are causing anisotropic line broadening. In this light, the apparent crystallites are interpreted in terms of a physical model by using ellipsoidal crystallites that are described by two distinct axis, such as the axial and equatorial ones. An isotropic model was described the extant of dislocation, distortion (micro-strain) within the crystal structure.

Results

Optical microscopy

In Appendix Table 3, the results of the histological analyses are reported. In Contemporary site, the 70% of bones appear well preserved (high OHI sub-class): the osteon structures are well recognizable, and the typical signs of bone diagenesis are absent (Fig. 1a). On the contrary, 80% of Late Roman bones appears badly preserved (low OHI sub-class) (Fig. 1b), exhibiting a massive erosion of the tissue, owing to fungal and bacteria actions. VS (Viale Sabotino) and CG (Ca' Granda) bones, although belonging to Modern Age, show differences in their state of conservation: CG bones are better preserved than VS bones, yielding 30% and 17% of well-preserved tissue, respectively. No bones from the CG site have a low histological conservation index, whereas about 67% of VS samples have an OHI ranging 0–1.

Scanning electron microscopy and electron microprobe in wavelength-dispersive mode

The results achieved by OM are confirmed by backscattered electron images, which allowed detection of morphological differences inside the osteonic structures and qualitative assessment of mineral changes. In Contemporary bones, the mineral changes of successive concentric lamellae of primary and secondary osteons can be easily recognized owing to their different gray scale (Fig. 1b). Grooves (or tunnels) produced by fungi penetrating into the bone (dark-grayish color) are observed in all of the investigated samples (Fig. 2). In particular, in Late Roman and Modern bones, a wide diffusion of bacterial colonies, leading to small pores and thin channels surrounded by bright areas, is detected (Fig. 1d). From BSE-SEM images, the TP, related to both vascular canals (i.e., Haversian and Volkmann canals) and diagenesis, can be qualitative observed. In particular, the vascular CP is characterized by large and well-rounded pores, whereas the DP is mainly constituted by small voids with an irregular shape. 2D imaging provides a partially distorted estimate of the bone total porosity, because it allows the visualization of the bone features and diagenetic alterations on a surface only. For such a reason, a high-resolution 3D inspection is necessary to get insight into the evolution of the actual natural and diagenetic porosity throughout the bone volume. In this view, the quantitative results of bone porosity achieved by SR-μCT will be given and discussed in the next paragraph.

Furthermore, the chemical analyses performed on selected points of preserved bone tissue of two samples with different ages (*CM*_8 and *UC*_7) show similar compositions in terms of major oxides (Table 1), within the uncertainties. Conversely,

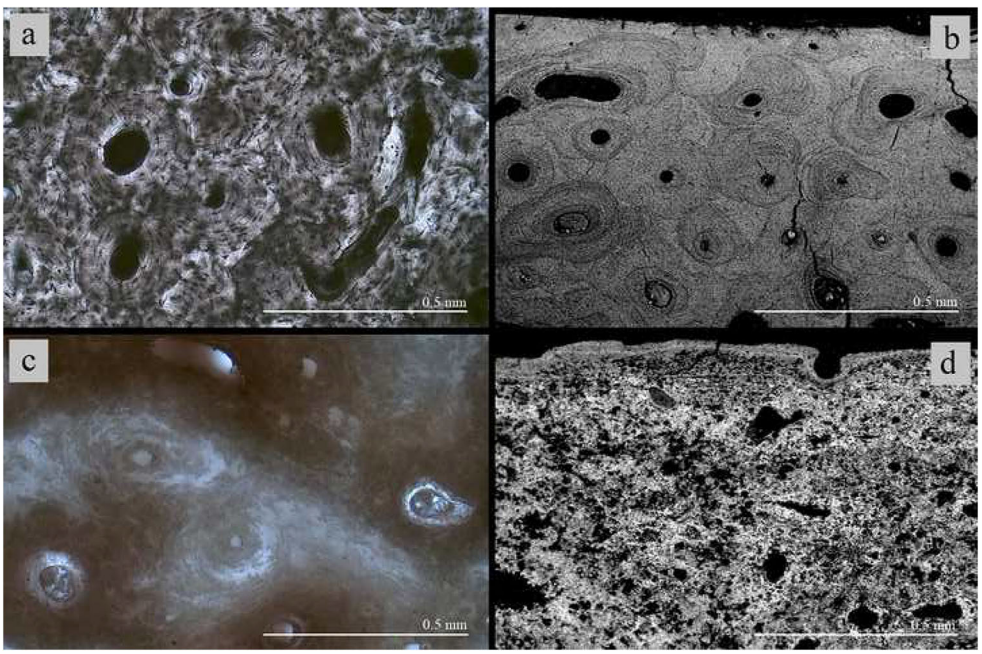

Fig. 1 OM and SEM micrographs: well-preserved bone tissue in the *CM*_10 sample (OHI 4–5), by OM (a) and BSE-SEM (b); badly preserved bone tissue in the *UC*_1 sample (OHI 0–1), by OM (c) and BSE-SEM (d)

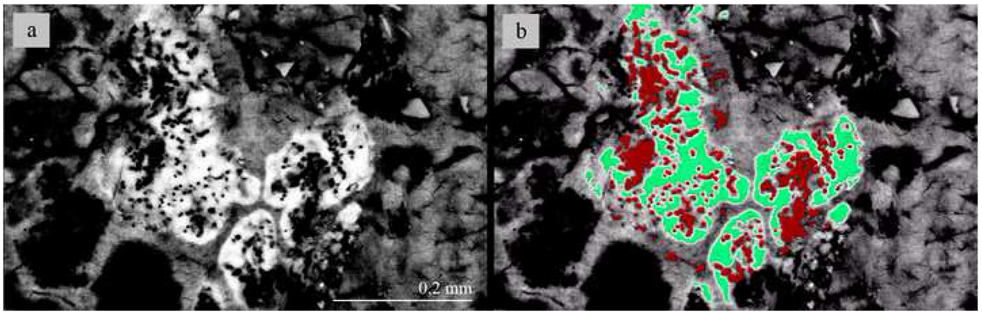

Fig. 2 Detail of microscopic damage produced by microorganisms in BSE-SEM (a). The resulting recrystallization and the voids produced by microbial action are highlighted in green and red, respectively (b)

CM_8 exhibits a higher content of minor oxides (i.e., with concentrations < 1 wt%). Additional analyses in the inner parts of the vascular canal pores prove high SO_2 content in *CM_8* (9–13 wt%).

In *UC_7*, an increase of CaO and a decrease of P_2O_5 are observed, corresponding to a higher Ca/P ratio, with respect to *CM_8*. Note that the two samples show low totals (75 wt%), probably due to the bone bulk composition consists of 30% of organic carbon, lipids, and water, which are out of the explorable range.

Synchrotron X-ray micro-tomography

Figure 3 shows the volume rendering performed on Contemporary (*CM_1*) (a) and Modern (*VS_8*) (b) specimens, exhibiting different degrees of bone preservation. The skeletonized volume (Fig. 3 a.2 and b.2) and the maximum inscribed spheres (Fig. 3 a.3 and b.3), which were used to determine the vascular canal connectivity and diameter, are highlighted.

The quantitative analysis performed on SR-μCT images indicates that the highest fraction of TP occurs in Contemporary samples (16%) (Fig. 4), and the lowest one (12%) in Late Roman bones. Although belonging to the same Modern Age, VS bones exhibit an increase in TP with respect to CG bones (15% and 10%, respectively).

The percentage of vascular CP on TP linearly decreases from Contemporary (84%) to Modern (46–37%) and Late Roman bones (30%). On the contrary, DP progressively increases from Contemporary to Modern and Late Roman samples, from 16 up to 70%. Only the CPs of Contemporary bones are linearly correlated to TPs. Additionally, in Late Roman and Modern bones, a high intra-site variability is observed in comparison with Contemporary bones.

The morphometric analysis on vascular canals' volume, reported in Appendix Table 4, shows a large number of mesopores (volume pores ranging from 1.0×10^{-05} to 1.0×10^{-03} mm^3) in all bones of the sites examined. Figure 5 proves also that only Contemporary bones reveal a bimodal volume-size distribution (VSD) of the vascular canals, leading to two main pore

Table 1 Electron microprobe analyses on preserved bone tissue of *CM_8* and *UC_7* samples (wt%). *bdl*, below the detection limit; *e.s.d.*, estimated standard deviation. Each result is calculated as an average of 30 points

	Preserved bone tissue on *CM_8*		Preserved bone tissue on *UC_7*	
	wt (%)	e.s.d.	wt (%)	e.s.d.
CaO	41.31	1.36	44.16	1.33
P_2O_5	32.51	1.64	30.7	3.86
FeO	0.03	0.03	0.03	0.03
Al_2O_3	bdl	-	0.04	0.01
Na_2O	0.87	0.07	0.45	0.05
K_2O	0.09	0.02	0.01	0.01
SiO_2	0.01	0.01	0.05	0.04
MnO	0.01	0.01	bdl	-
MgO	0.43	0.05	0.34	0.08
SrO	0.04	0.04	0.03	0.03
BaO	0.03	0.02	0.04	0.02
SO_2	0.48	0.12	0.56	0.08
Cl	0.05	0.03	0.06	0.01
Total	75.86	2.63	76.47	4.63
Ca/P	1.61		1.82	

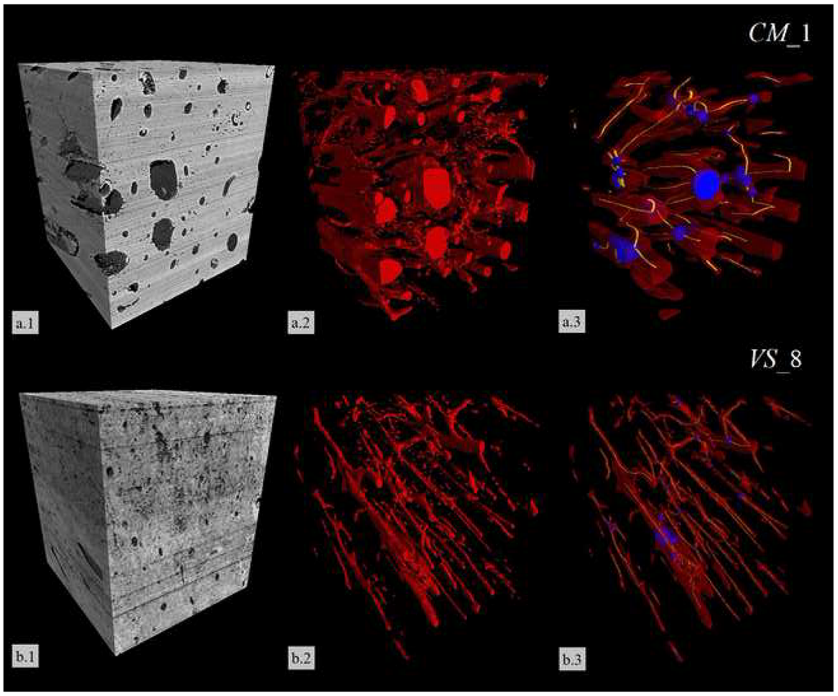

Fig. 3 Volume rendering (VOI = $4 \times 4 \times 4$ mm^3, $900 \times 900 \times 1100$ voxels) of well-preserved bone samples of (a) Contemporary age (*CM*_8) and (b) diagenetically altered bone sample of Modern age (*VS*_8). For each sample, the related VOI are shown: (1) raw (as reconstructed) images; (2) vascular canal networks (in red); (3) filtered vascular canal networks employed for morphological analysis with skeletonized volume (in yellow) and maximum inscribed spheres used to calculate the vascular canal pore diameters (in blue)

distributions into the meso- and macro-pores, respectively. On the contrary, the VSD curves plotted for Late Roman and Modern specimens exhibit a decrease of macro-pores, mainly in UC bones. Appendix Table 4 points out a high vascular canal pore connection in Contemporary bones ($\chi_V < 1$), whereas in Late Roman and Modern specimens, connectivity seems almost negligible ($\chi_V > 1$). A decrease of the vascular canal diameter from 0.125 to 0.020 mm is observed passing from Contemporary to Modern and Late Roman bones.

Fourier transform infrared spectroscopy

The set of spectra obtained by FT-IR spectroscopy, and reported in Fig. 6, shows a high absorbance peaks at ν_1Amide I and $\nu_2(CO_3^{-2})$ in Contemporary bones, which decrease in Modern and Late Roman bones. The calculated amide I to phosphate ratio decreases from 0.73 to 0.20 from Contemporary to Late Roman bones, as reported in Appendix Table 5. Modern bones have intermediate value

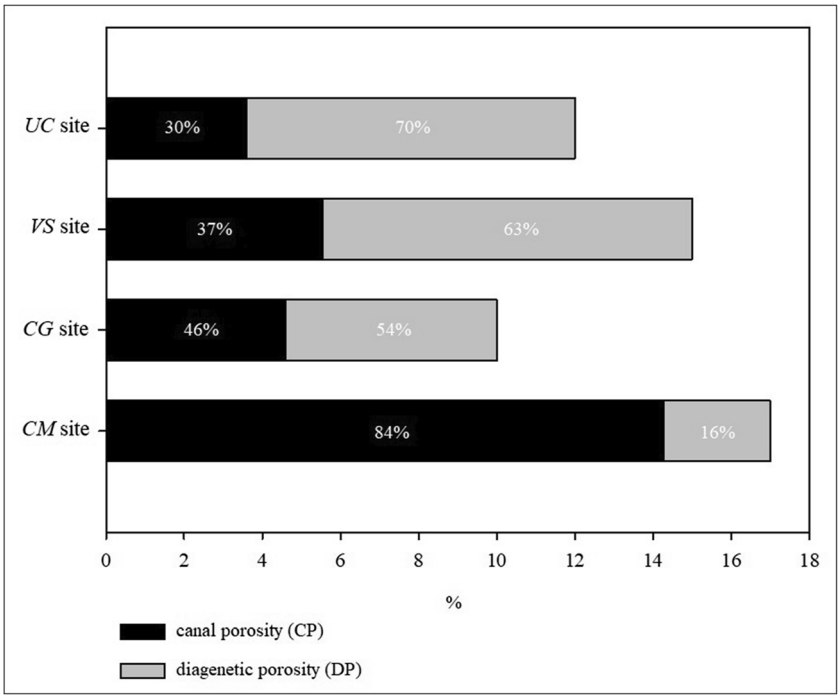

Fig. 4 Percentage of total porosity (TP) detected in each site. On scale bar, the percentage fractions of vascular canal (CP) and diagenetic porosity (DP) with respect to the total porosity are reported. (e.d.s. 10% for UC and CM samples and 30% for VS and CG samples)

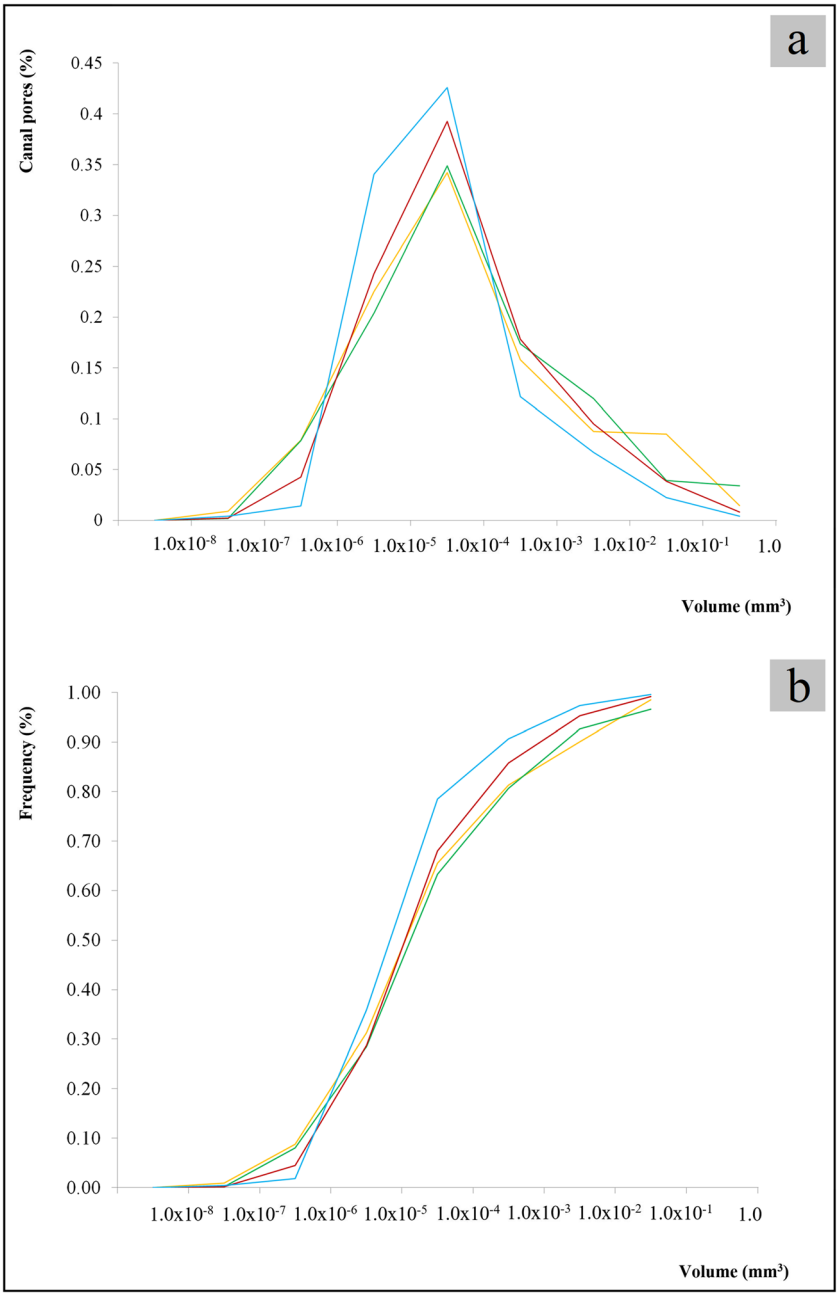

Fig. 5 (a) Pore distribution of the vascular canal pore volumes and (b) cumulative frequency distribution of vascular canal pore volumes

(0.56 in CG and 0.3 in VS site). As a consequence, the resulting fraction of organic matter decreases from 29 in CM to 18 wt% in UC bones. In Modern bones, the calculated fraction of organic matter takes intermediate values between those observed in Late Roman and Contemporary ages, ranging from 20 to 25 wt%. Likewise, the carbonate to phosphate ratio assumes its highest values in Contemporary bones (0.52) versus Modern (0.44 in CG and 0.40 in VS) and Late Roman bone (0.34). On the contrary, the crystallinity index (IRSF) increases from Contemporary bones (2.7) to Modern (2.8) and Late Roman bones (2.9). On the basis of the IRSF, the calculated mean crystal length of bone mineral shows an increase from Contemporary (39 nm) to Modern (41–42 nm) and Late Roman samples (45 nm). An inverse correlation can be established between IRSF and the amide I content, and the same holds between CO_3^{-2} content and IRSF values. Such results are set out in Appendix Table 5.

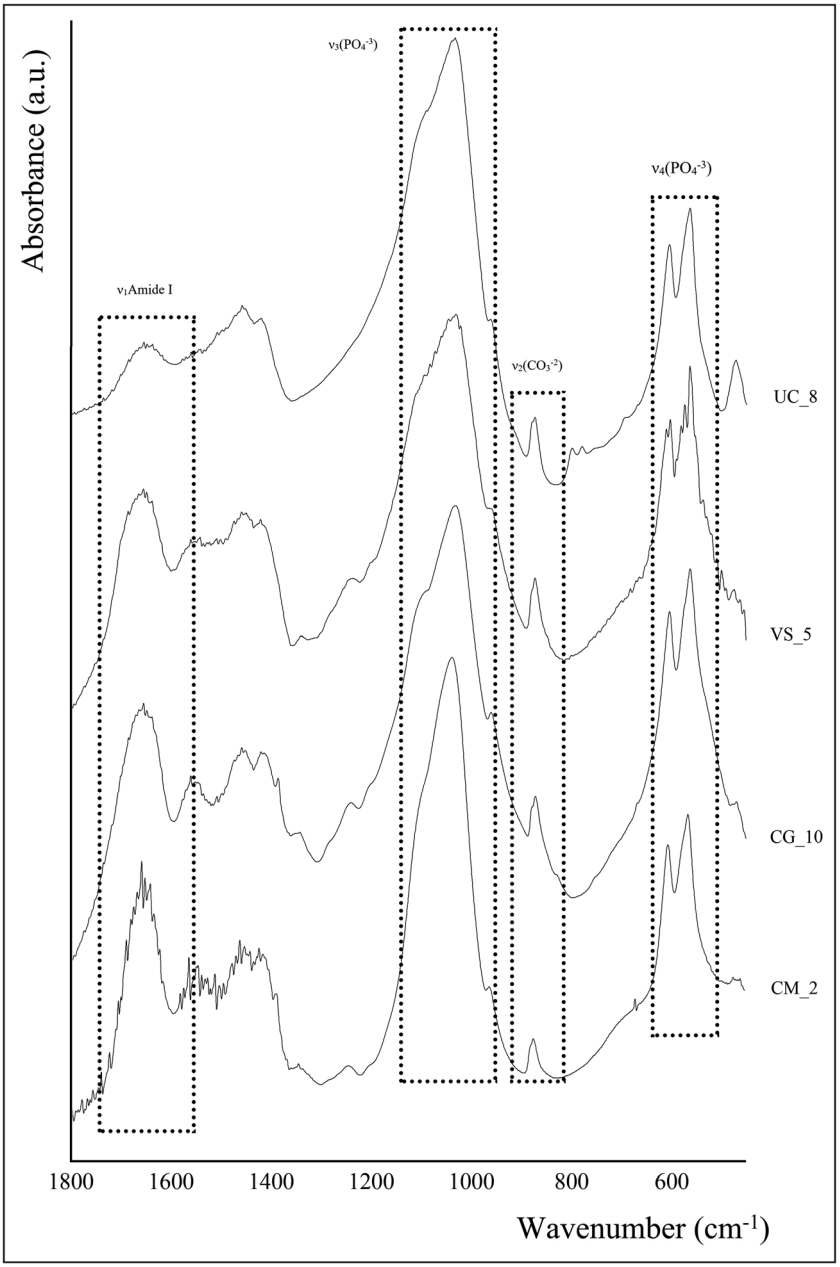

Fig. 6 FT-IR spectra of Late Roman (*UC*_8), Modern (*VS*_10, *CG*_8), and Contemporary (*CM*_10) bones. *CG*_8 had the highest absorbance peaks of collagen band at about 1653 cm^{-1} and CO_3^{-2} at 873 cm^{-1}

X-ray powder diffraction

Figure 7 displays an example of XRPD pattern, in which the observed (dashed line), calculated (continuous line), and difference curves (bottom line) of a Late Roman sample (*UC*_8) are shown. All the samples have phase compositions mainly constituted by hydroxyapatite associated with minor amounts of calcite and quartz. No evidences of brushite and apatite are detected. Crystallographic refinements of the hydroxyapatite cell parameters reveal that the average unit cell volumes are quite similar in all the samples (ranging from 530 to 533 $Å^3$), within the experimental uncertainties; the largest cell volume (533 $Å^3$ in mean) is observed in the oldest sample, mainly due to an increase of the *a*-cell parameter.

The quality of diffraction patterns is not so high as to allow refinement of the atomic thermal parameters, site occupancies, and atomic positions, but differences in the micro-structural properties of hydroxyapatite are observable.

As for domain size, both isotropic and anisotropic models were used to calculate its contribution to the line broadening. The least satisfactory results were obtained employing isotropically shaped crystallites (R_{wp} and GoF of 12.3 and 3.2) and the fit quality, especially in the 24–35° 2θ range (Cu radiation), were very poor. Conversely, the uniaxial

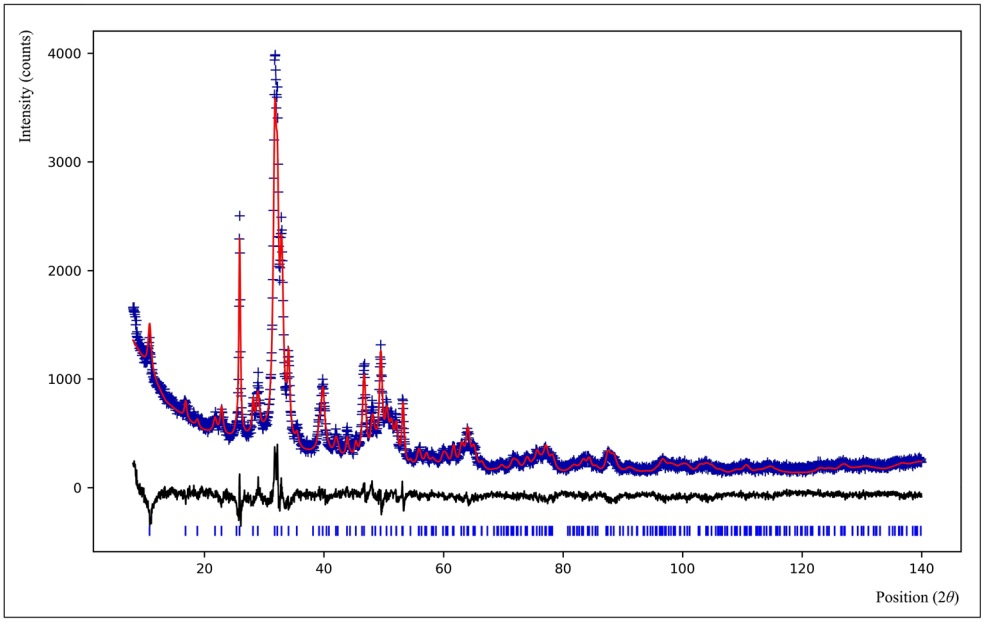

Fig. 7 XRPD pattern of Late Roman bone (*UC_8*). The calculated (red line) and observed (blue line) patterns are highlighted, and the residual resulting from Rietveld refinement is also displayed at the bottom. The main (hkl) Bragg peaks are reported

model provided a significant improvement (R_{wp} and GoF of 7.8 and 1.9), thus confirming that this model is more appropriate to describe the crystallite shape. All the more so taking into account that the Bragg peaks in the XRPD profiles show signs of strong anisotropy, the *00l* reflections are noticeably sharper than the others, suggesting that the coherent diffraction domains preferentially align along [001]. From Appendix Table 6, we stress that: (i) the average size of the diffracting domain of hydroxyapatite is nanometric, thus suggesting that its crystal structure is far from the ideal one (Wopenka and Pasteris 2005); (ii) the equatorial component of the uniaxial model is quite similar in all the samples even though the highest value is observed in Contemporary bones (*CM_2*); (iii) large differences in terms of axial values measured along [001] are visible: for *CG_10* and *VS_5*, the value is 170 Å, whereas in *CM_2* and *UC_8*, it rises up to 420 Å, thus suggesting that the coherent diffraction domains in the Late Roman and Contemporary bones are larger and/or less defective than Modern ones (i.e., *VS_5* and *CG_10* had intermediate values).

Micro-strain, which affects the profile broadening of peaks, was taken into account using the generalized micro-strain model implemented in GSAS-II and employing for simplicity an isotropic model. Although an anisotropic model would better describe the crystallite complexity, in terms of preferred distortion, dislocation, and planar defects, it was not used because of the correlations occurring between refinement parameters and leading to unreliable results. Notwithstanding the high dispersion and statistical uncertainty, the micro-strain values from the isotropic model suggest that the anisotropy of hydroxyapatite is more pronounced in Contemporary bone (*CM_2*) than in Late Roman and Modern bones (*UC_8*, *VS_5*, *CG_10*) (Fig. 8).

Discussion

The results from adult human skeletons suggest that a correlation between alterations (in terms of microstructures and physical-chemical features of the organic and mineral fractions) and time elapsed since death is not easily recognizable. Nevertheless, a multi-analytical approach can help (i) reveal the typical constituents of bone degradation due to diagenetic processes and (ii) provide information on the influence of the post-mortem burial settings on the bone preservation.

Histology

Optical microscopy observations bring to light a progressive level of degradation from Contemporary to Modern and Late Roman bones, although a large intra-site variability is observed in terms of OHI values (Nielsen-Marsh and Hedges 2000; Guarino et al. 2006). In Contemporary bones, the typical micro-structural features usually found in fresh bones are well recognized: (i) primary osteons, constituted by concentric lamellae surrounding the Haversian canals, as well as Volkmann canal interconnections; (ii) secondary osteons, which intersect the primary ones; (iii) canaliculi and osteocyte lacunae (Fig. 1a, b). Conversely, Modern and Late Roman bones are affected by bioerosion (Fig. 1c, d), and the microbial focal destruction (MFD) is widespread over the whole thin sections, especially in Late Roman bones. The significant variability in the OHI values within each site does not allow definition of a linear relationship between time elapsed since death and bone preservation degree, and suggests that, at the same environmental conditions, human remains can react differently even under the same burial setting. The largest heterogeneity is observed in VS sites, where OHIs are distributed

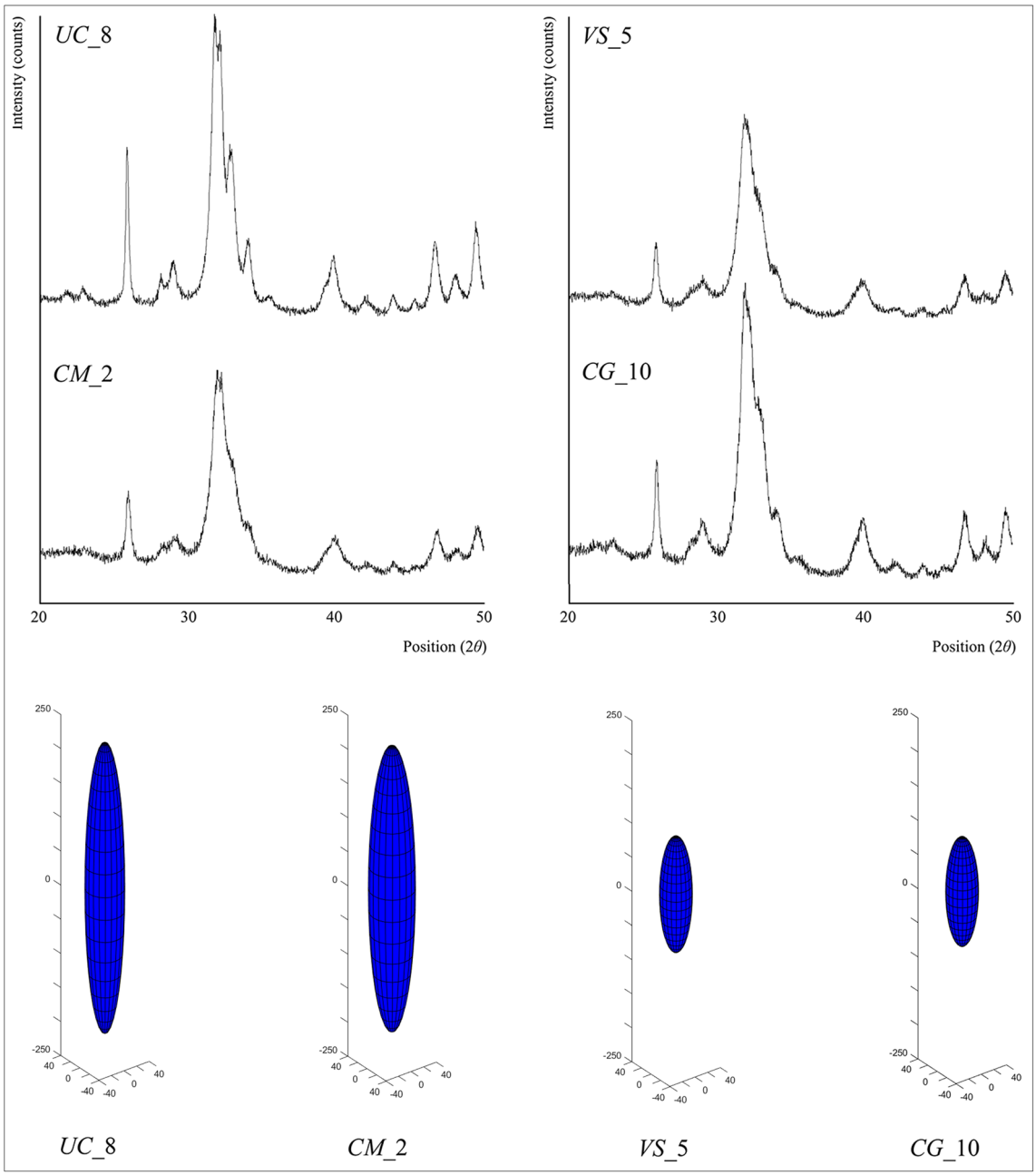

Fig. 8 Inset of the most representative peaks of hydroxyapatite carried out from XRPD measurements performed on Contemporary (*CM*_2), Modern (*CG*_10 and *VS*_5), and Late Roman (*UC*_8) bones. An indicative 3D model of the shape of hydroxyapatite crystallites, elongated along the *c*-axis, was also reconstructed from the difference among hkl peak broadening for each bone (measures in ångström)

into the three sub-classes, whereas the UC bones exhibit the lowest OHI variance, with almost all of the samples falling into the low OHI sub-class. CM and CG sites present 30% of variability, having samples in the medium and high OHI sub-classes. Confined areas of destruction, produced by microbes on both external and internal cortical borders, are observed also in CM samples, wherein fungal attacks cause large and irregular grooves penetrating into the bones and resulting in dark-grayish tunnels. Bacterial attacks yield severe destruction of the bone microstructure, promoting the occurrence of small pores and thin channels surrounded by a matrix characterized by the highest BSE intensity values in Fig. 2 and by a calcium-phosphate bearing chemical composition. The latter may be considered the result of a recrystallization of the original bone mineral, hereafter reported as secondary CHA (Hackett 1981; Hedges et al. 1995; Child 1995a, 1995b; Bell et al. 1996; Hedges 2002; Turner-Walker et al. 2002; Jans et al. 2004; Turner-Walker and Jans 2008; Fernández-Jalvo

et al. 2010; Müller et al. 2011). All this confirms that bioerosion starts even 3 months after death (Hedges et al. 1995; Bell et al. 1996; Boaks et al. 2014; White and Booth 2014) and cannot be considered a peculiar feature only of the oldest bones. Therefore, the extent of microbial action is not related to the chronological age of an archaeological bone (i.e., a good histological conservation has been observed also on bone sections of fossil animals from Silurian to Pleistocene in age, Trueman and Martill 2002; Turner-Walker 2012). Although bone histology seems to be more dependent on the burial environmental fluctuations than on the time elapsed since death, there seems to be no apparent relationship between the degree of bone micro-structural preservation and the kind of environment from which the bones come (Bell et al. 1996; Jackes et al. 2001; Jans et al. 2004; Guarino et al. 2006; Nielsen-Marsh et al. 2007; Turner-Walker and Jans 2008; Hollund et al. 2012; Boaks et al. 2014; White and Booth 2014; Booth and Madgwick 2016; Morales et al. 2017). Butchered archaeological bones appear often free of bioerosion, whereas bones from fully articulated skeletons show extensive damages due to bacteria. All this hints at a prominent impact of endogenous gut bacteria in the decomposition process (Huisman et al. 2017; Brönnimann et al. 2018). Consequently, a rapid skeletonization likely limits the degree of putrefactive decomposition and of the related microbial damage (Hollund et al. 2012).

3D porosity

In addition to histological evaluation, bone porosity appears as an important marker of post-mortem changes (Smith et al. 2008; Turner-Walker et al. 2002; Nielsen-Marsh and Hedges 2000; Nielsen-Marsh and Hedges 2000). Figure 4 shows that the high porosity of Contemporary bones is mainly due to the vascular canals, whereas in Late Roman and Modern specimens, the pores result from diagenetic alteration. A progressive general reduction of the volume of vascular canal fraction from Contemporary to Modern and Late Roman bones (from macro-pores to mesopores in Fig. 5), as well as a marked reduction of vascular canal diameter, takes place as diagenesis proceeds (see Appendix Table 4), in keeping with Nielsen-Marsh (Nielsen-Marsh and Hedges 2000). Furthermore, a general loss of intervascular canal connections is shown in Fig. 3: only in Contemporary bones, the vascular canal sizes are highly preserved (0.125 mm in diameter), as well as the vascular canal interconnections ($\chi_V < 1$) (longitudinal, transverse, and oblique). On the contrary, a marked increase of diagenetic pores was observed from Contemporary to Modern and Late Roman bones attributable to the chemical degradation of organic matrix as well as to the dissolution of bone mineral, mainly promoted by microbial action (Nielsen-Marsh and Hedges 2000; Turner-Walker et al. 2002; Robinson et al. 2003; Smith et al. 2008; Müller et al. 2011). SR-μCT results point to intra-site variability, mainly in Modern bones where a large estimated standard deviation of bone total volume porosity is observed (Fig. 4). The observed heterogeneity in terms of bone porosity and histological deterioration in VS and CG bones is the result of an interplay between time elapsed since death and local burial conditions.

Consequently, even if porosity gives a clear and direct indication of the degree of diagenetic changes and might appear as a powerful tool for assessing the state of bone deterioration, its variability makes it a poor marker of age (Hedges et al. 1995; Nielsen-Marsh and Hedges 2000; Jackes et al. 2001; Reiche et al. 2002; Turner-Walker et al. 2002; Fernández-Jalvo et al. 2010; Abdel-Maksoud and Abdel-Hady 2011).

Organic and carbonate contents and crystallinity measurements

The diagenetic alteration of human bones is also well assessed by FT-IR spectroscopy, suggesting a straightforward relationship between chemical and structural modifications of the organic and mineral fractions and the time elapsed from death (Winer and Bar-Yosef 1990; Person et al. 1995; Abdel-Maksoud and Abdel-Hady 2011). In particular, Contemporary bones exhibit the highest absorbance of amide I and carbonate abundance, with respect to Modern and Late Roman bones (Fig. 5). The amide I to phosphate ratio decreases from 0.73 to 0.20 (see Appendix Table 5), passing from Contemporary to Modern and Late Roman specimens. Furthermore, the carbonate to phosphate ratio decreases from 0.52 (CM bones) to 0.34 (UC bones), in keeping with an inverse correlation proven to hold between preservation of the organic fraction and crystallinity (Turner-Walker et al. 2002; Lebon et al. 2011). This confirms that as the diagenesis proceeds, the degradation of the organic phase promotes mineral changes, favoring the recrystallization of the bone mineral fraction (Trueman et al. 2004; Reiche et al. 2010; Rogoz et al. 2012). However, this process is extremely slow and may be accelerated only by a massive microbial decay, heating, and/or extreme acid environments, for it to have a relevant impact on the bone structure (Collins et al. 2002).

Despite the high heterogeneity of collagen preservation within single bones of archaeological samples reported in previous works (Reiche et al. 2010; Lebon et al. 2011; France et al. 2014; Lebon et al. 2016), our results evidence a positive correlation between the availability of organic content and the sample age. Moreover, the distribution of carbonate content in our samples seems to be a reliable marker of the diagenetic history of bone over time (Lebon et al. 2014).

An inverse correlation between carbonate content and IRSF confirms that the carbonate loss leads the bone mineral to take the thermodynamically stable form of secondary CHA (Trueman et al. 2004). Note that an alkaline pH is required to

observe bone mineral recrystallizes into secondary CHA (the so-called recrystallization window) (Berna et al. 2004).

The highest IRFS values are observed in Late Roman bones (2.9) in association with an average crystal length of 45 nm. Modern samples exhibit similar values in terms of IRSF and crystal length (2.8 and 41–42 nm, respectively) whereas the Contemporary ones have the lowest crystallinity and crystal length figures (2.7 and 39 nm, respectively). The slight increment of both IRSF and mean crystal length from Contemporary to Ancient bones may be caused by the simultaneous dissolution of small crystals and growth of larger ones (Molin et al. 2002; Trueman et al. 2004; Lebon et al. 2011; Rogoz et al. 2012), in agreement with the Ostwald ripening mechanism (Wei et al. 1999; Arantes et al. 2018). However, in comparison with the reference data, which report an increment of the IRSF up to 4.5–5.0 on fossil and heated samples (Reiche et al. 2002; Trueman et al. 2004; Trueman et al. 2008; Chadefaux et al. 2009b; Squires et al. 2011; Müller et al. 2011; Hollund et al. 2013; Stathopoulou et al. 2013; Beasley et al. 2014; Lebon et al. 2014; Monge et al. 2014; Margariti et al. 2019), our IRSF values in Modern and Late Roman samples suggest a partial involvement of bone mineral in the diagenetic process (Reiche et al. 2010). Therefore, we gather that only in the presence of a significant increment of the time elapsed since death (> 2000 years old), mineral changes can be well revealed in the bone structure.

Mineralogy and chemistry

Despite the abovementioned heterogeneity, no difference in terms of mineralogical composition can be detected among all the investigated samples. Secondary CHA appears as a major phase and it is associated with minor contents of calcite and quartz. Calcium carbonate occurs as authigenic mineral inclusions that fill bone voids and result from diagenetic processes (Prieto-Castelló et al. 2007; Piga et al. 2011; Rogoz et al. 2012). The quartz in the internal cavities of Late Roman and Modern bones is considered a "mineral inheritance," whose origin depends on the mineralogical features of the depositional sediment (Person et al. 1995; Monge et al. 2014; Margariti et al. 2019).

Chemical and crystallographic changes of secondary CHA seem to be correlated to diagenetic processes. The bone mineral fraction is poorly crystalline apatite with a marked increase in the Ca/P mole ratio from Late Roman to Contemporary bones (1.82 and 1.61, respectively), thus differing from the theoretical value of pure hydroxyapatite (1.67). The enrichment in Ca^{2+} ions in UC sites may be attributed to a bone alteration which results in the recrystallization of the original mineral phases into a thermodynamically more stable form (secondary CHA) (Rogoz et al. 2012; Stathopoulou et al. 2013; Keenan et al. 2015; Margariti et al. 2019).

The higher contents in minor species like Na_2O and K_2O in CM bones may be associated with the ionic substitutions of Na^+ and K^+, in place of Ca^{2+} in the bone mineral structure. This appears more likely in in vivo bones because of non-stoichiometric calcium-deficient bioapatite (Wopenka and Pasteris 2005). These species can be considered markers pointing to a diet rich in animal and/or plant components, even though an exogenous origin cannot be excluded. In addition, the large contents of SiO_2 and SO_2 in UC bones are related to the substitution of Si^{4+} and S^{2+} in place of P^{3+} during the decomposition of bones probably taken from the burial setting (Wopenka and Pasteris 2005; Keenan et al. 2015; Abdel-Maksoud and Abdel-Hady 2011; Abdel-Maksoud and El-Sayed 2016; Margariti et al. 2019). In particular, the significant content of SO_2 detected inside the vascular canal pores of Contemporary bones may be referred to sulphuric acid occurring as a residue of decomposition processes (Keenan et al. 2015).

The cell parameters of the CHA are comparable with the ones reported in literature (Piga et al. 2009, 2013), suggesting an increase in the cell volume as the diagenesis increases. The largest values observed in the Late Roman bones reflect the high content of CaO in its crystal structures.

The similar values for *c*-axis reported for Contemporary and Late Roman bones, in comparison with reference samples (Margariti et al. 2019), suggest a global improvement of the bone crystallinity with diagenesis, as it has been observed in association with the post-mortem burial or carbonization process, because it takes place when a bone starts losing its organic material (Person et al. 1995; Reiche et al. 2002; Prieto-Castelló et al. 2007; Abdel-Maksoud and Abdel-Hady 2011; Monge et al. 2014).

In the present study, a *hkl*-dependent broadening of the Bragg peaks is visible in powder diffraction patterns and has often made it difficult to model the peak shape in Rietveld analysis. Such anisotropic peak broadening may be due to a variety of reasons, such as anisotropic particle shape, occurrence of stacking faults, and anisotropic strain. Despite a variance in the obtained results, significant differences in terms of domain size and micro-strain values are observed among the samples, suggesting a progressive loss of alignment along the *c*-axis in the Late Roman and Modern bones, with a consequent reduction of anisotropy.

In particular, the micro-structural features inferred from the profile analysis of XRPD patterns indicate that secondary CHA has a highly defective structure in all the samples, as suggested by the nanometric size of the coherent diffraction domains. The micro-structural features of the Late Roman samples confirm that the diagenesis induces the recrystallization of a newly formed hydroxyapatite which exhibits a high crystallinity (i.e., large domain size) at the micro-scale, with respect to the Modern and Contemporary ones. Note that in the Contemporary bones, large domain sizes are associated

with high values in terms of micro-strain, suggesting a high density of defects and dislocations within the coherent domains.

Diagenetic pathways as a function of elapsed time since death and burial context

The multidisciplinary approach used in the present study suggests that in the oldest bones of the UC site, a massive erosion of bone tissue at histological scale took place. An increase of diagenetic porosity at the expenses of the natural one is observable, with a reduction of size, density, and interconnections between vascular canals. The amounts of protein and carbonate are significantly reduced, as well as the bone mineral appears recrystallized. Diagenesis also induces the recrystallization of a newly formed secondary hydroxyapatite exhibiting a nearly free-defect structure, along with a progressive loss of alignment along the *c*-axis, with a consequent reduction of original anisotropy.

On the contrary, Contemporary bones of the CM site show an excellent histological preservation. Natural vascular canals appear similar to those of fresh bones. The bone tissue bears large contents of proteins and carbonate, and a low crystallinity index. The bone mineral has a nanometric size of the coherent diffraction domains, with high density of defects and dislocations in the structure. The bone crystals are also aligned along the *c*-axis and preserve their anisotropic shape.

In this case, the high preservation of the CM bones that resemble fresh bones appears related to the use of coffins, wherein the bodies were buried and which protected the corpses against weathering, so that only after putrefaction of soft tissues, the bones became progressively affected by decay processes (Kendall et al. 2018 and references therein).

As for Modern bones, although they belong to the same chronological age, our results confirm they underwent different weathering processes related to the local conditions of the burial settings. The samples of the VS site were recovered from a mass grave, whereas the bones of the CG site were housed in an ossuary inside a crypt. Therefore, both sites preserve commingled human remains, but they were exposed to different conditions of pH, temperature, humidity, chemical, and microbiological environments, thus leading to different bone conservation levels after death. The main differences in conservation were observed at histological scale, where CG bones appear well preserved compared with VS bones and exhibit an extensive microbial activity. At the same time, the higher modifications in terms of natural and diagenetic porosity were observed in VS bones only, whose alterations resemble those previously detected on UC bones. Conversely, CG bones display a natural vascular canals' morphology similar to that observed on CM bones, with few signs of diagenetic porosity.

All Modern bones have a similar alteration of bone mineral, collagen, and carbonate content, as observed by both FT-IR and XRPD analyses.

Therefore, this research points out that bones from the same chronological age differ from each other only in terms of microstructure and porosity. The organic and mineral phases appear more sensitive to the time elapsed since death than to the conditions of the burial context; the bone histology, in turn, seems poorly correlated to the organic and mineral fractions.

Depletion of proteins along with chemical and mineral changes in bones after death occurs not completely mediated through microbial actions, which might play a major role in histological alterations. In this view, other factors are able to promote or inhibit the conservation of the organic and mineral bone components. For instance, extreme acidity or alkalinity condition of soil pH, high temperature, and active hydrology (cyclical wetting and dying regimes) promotes the swelling and shrinking of collagen fibers, as well as dissolution and recrystallization of minerals (Kendall et al. 2018 and references therein).

The high histological preservation of CG bones may have been promoted by the conditions of the crypts, which protected bones against climate (soil, rainfall), maintaining a constant low-temperature and an anoxic micro-environment (Nielsen-Marsh and Hedges 2000), thus inhibiting the development of microbiological action. Conversely, the similar histological degradation observed in bones of UC and VS site hints at more aggressive conditions of burial environment in VS site, with acidic soil and hydrological fluctuations (Nielsen-Marsh and Hedges 2000), impairing conservation of bone tissue, which resembles that of the most ancient site.

Conclusions

The present research aims to contribute to a better understanding of the complex correlations among factors that affect human bones during the diagenetic process (namely burial environment and time elapsed since death). In particular, the work focuses on how the organic and mineral components influence each other and the resulting micro-structural features of the human bones.

The results highlighted a lower correlation between the preservation of micro-structural assessment and the degree of conservation of organic and mineral fractions than expected. In particular, a relationship was observed between the conservation of the organic and mineral fractions and the time elapsed since death. On the other hand, the micro-structural bone features, in terms of porosity and histological assessment, seem to be more influenced by the environmental burial conditions.

Generally, as diagenesis proceeds, bone undergoes several different pathways of deterioration as follows:

1. A progressive attack of microbes (bacteria and fungi) leading to a complete destruction of the osteon's structures and to an increase in the diagenetic porosity;
2. A general reduction of the vascular CP and of the vascular canal diameters and their connections;
3. A decrease of the organic and carbonate fractions with time, thus promoting the recrystallization of bone mineral into a thermodynamically more stable form of secondary CHA. The growth of this resulting newly formed mineral phase follows the Ostwald ripening process and this latter yields a general increase of its crystal size;
4. A marked increase in the Ca/P mole ratio in CHA crystals is attributed to the recrystallization of the original mineral phases (secondary CHA);
5. A progressive loss of alignment along the *c*-axis of CHA, with a consequent reduction of anisotropy as well as an increase in the domain size as diagenesis proceeds.

Nevertheless, a discrete variability was found among bones from the same assemblage, mainly in the Modern sites, especially in terms of histological appearance and degree of preserved natural versus diagenetic porosity. The preservation degree of modern bones (VS and CG) appears similar to the one detected in Late Roman (UC) and Contemporary (CM) samples. The work highlights the high heterogeneity of diagenetic process, because of an interdependence between the time elapsed since death and the burial local environment. In particular, the relationship between the conservation of organic and mineral phase and the histological preservation is not very close.

In this light, a complete understanding of the diagenetic process requires a multidisciplinary approach, taking into account the potentialities and limitations of each of the employed analytical techniques. The combination of a multidisciplinary approach is useful to remove possible ambiguities and/or uncertainties in defining the preservation degree of bone materials. In particular, a 2D imaging analysis performed by optical and electron microscopy may provide an unfaithful assessment of bone diagenesis. On the contrary, the 3D high-resolution synchrotron micro-tomography gives the actual image of the bone inner parts with an extraordinary level of details of its microstructure. In particular, morphometric vascular canal network is an important issue, since a low image resolution tends to underestimate vascular pores and a high resolution of at least 1 μm is required to achieve a precise quantification of such an observable (Cooper et al. 2003; Palacio-Mancheno et al. 2014).

Acknowledgments The authors would like to thank all staff of SYRMEP beamline at the Elettra synchrotron facility during data collection and the staff of EMP and XRD laboratories of Università degli studi di Milano, Dipartimento di Scienze della Terra "Ardio Desio," for their precious technical support for data collection.

Author contribution VC and NM wrote the main manuscript text. LP and AP assisted in data interpretation and revision of the manuscript. VC and VD performed EMP analysis and interpreted the results. VC and LT performed SEM analysis and elaborated the data. VC, NM, and MC performed XRD and elaborated the data. VC and CC elaborate the data of OM. VC, NM, and LM performed SR-μCT analysis and interpreted the results. VC and FB performed FT-IR analysis and elaborated the data. All authors reviewed the manuscript.

Funding information This work was supported by Fondazione Fratelli Confalonieri, Milan (Italy).

Compliance with ethical standards Archaeological human bones were provided by LABANOF, Laboratorio di Antropologia e Odontologia Forense, of Università degli Studi di Milano (Milan, Italy), in accordance with Soprintendenza Archeologica Belle Arti e Paesaggio per la città metropolitana di Miano (Italy). Contemporary bones were provided in accordance with the Police Mortuary Rules (DPR 09.10.90 n8 285, art. 43) and thanks to an agreement between the municipality of Milan and the Department of Legal Medicine of Università degli Studi di Milano (Milan, Italy), unclaimed human remains can be used for scientific research.

Conflict of interest The authors declare that they have no conflict of interest.

References

Abdel-Maksoud G, Abdel-Hady M (2011) Effect of burial environment on crocodile bones from Hawara excavation, Fayoum, Egypt. *JCH* 12:180–189

Abdel-Maksoud G, El-Sayed A (2016) Analysis of archaeological bones from different sites in Egypt by a multiple techniques (XRD, EDX, FTIR). Mediterranean Archaeol. Archaeom. 16(2):149–158

Amarante A, Ferreira MT, Makhoul C, Vassalo AR, Cunha E, Gonçalves D (2019) Preliminary results of an investigation on postmortem variations in human skeletal mass of buried bones. Sci Justice 59(1:52–57

Ambrose SH, Krigbaum J (2003) Bone chemistry and bioarchaeology. J Anthropol Archaeol 22:193–199

Arantes TM, Coimbra LMM, Cristovan FH, Arantes TM, Rosa LLM (2018) Synthesis and optimization of colloidal hydroxyapatite nanoparticles by hydrothermal processes. J Braz Chem Soc 29(9):1894–1903

Assis S, Keenleyside A, Santos AL, Cardoso FA (2015) Bone diagenesis and its implication for disease diagnosis: the relevance of bone microstructure analysis for tge study of past human remains. Microsc Microanal 21:805–825

Beasley MM, Bartelink EJ, Taylor L, Miller RM (2014) Comparison of transmission FTIR, ATR, and DRIFT spectra: implications for assessment of bone bioapatite diagenesis. J Archaeol Sci 46:16–22

Beauthier JP, Lefevre P, Meunier M, Orban R, Polet C, Werquin JP, Quatrehomme G (2010) Palatine suture as age indicator: a controlled study in the erderly. J Forensic Sci 55:153–158

Bell LS, Skinner MF, Jones SJ (1996) The speed of post mortem change to the human skeleton and its taphonomic significance. Forensic Sci Int 82:129–140

Bello SM, Parfitt SA, De Groote I, Kennaway G (2013) Investigating experimental knapping damage on an antler hammer: a pilot-study using high-resolution imaging and analytical techniques. J Archaeol Sci 40:4528–4537

Berna F, Matthews A, Weiner S (2004) Solubilities of bone mineral from archaeological sites: the recrystallization window. J Archaeol Sci 31:867–882

Boaks A, Siwek D, Mortazavi F (2014) The temporal degradation of bone collagen: a histochemical approach. Forensic Sci Int 240:104e110

Booth TJ (2016) An investigation into the relationship between funerary treatment and bacterial bioerosion in european archaeological human bone. Archaeom. 58(3):484–499

Booth TJ, Madgwick R (2016) New evidence for diverse secondary burial practices in Iron Age Britain: a histological case study. J Archaeol Sci 67:14–24

Booth TJ, Redfern RC, Gowland RL (2016) Immaculate conceptions: micro-CT analysis of diagenesis in Romano-British infant skeletons. J Archaeol Sci 74:124–134

Boskey A (2003) Bone mineral crystal size. Osteoporos Int 14(suppl 5): s16–s21

Bradfield J (2013) Investigating the potential of micro-focus computed tomography in the study of ancient bone tool function: results from actualistic experiments. J Archaeol Sci 40:2606–2613

Brady AL, White CD, Longstaffe FJ, Southam G (2008) Investigating intra-bone isotopic variations in bioapatite using IR-laser ablation and micromilling: implications for identifying diagenesis? Palaeogeogr Palaeoclimatol Palaeoecol 266:190–199

Brönnimann D, Portmann C, Pichler SL, Booth TJ, Röder B, Vach W, Schibler J, Rentzel P (2018) Contextualising the dead-combining geoarchaeology and osteoanthropology in a new multi-focus approach in bone histotaphonomy. J Archaeol Sci 98:45–58

Brooks S, Suchey JM (1990) Skeletal age determination based on the os pubis: a comparison of the Acsadi-Nemeskeri and Suchey-Brooks methods. Hum Evol 5:227–238

Brun F, Dreossi D (2010) Efficient curve-skeleton computation for the analysis of biomedical 3D images. Biomed Sci Instrum 46:475–480

Brun F, Mancini L, Kasae P, Favretto S, Dreossi D, Tromba G (2010) Pore3D: a software library for quantitative analysis of porous media. Nucl Instrum Methods Phys Res A 615(3):326–332

Brun F, Pacilè S, Accardo A, Kourousias G, Dreossi D, Mancini L, Tromba G, Pugliese R (2015) Enhanced and flexible software tools for X-ray computed tomography at the Italian synchrotron radiation facility Elettra. Fund Inf 141:233–243

Caruso V, Cummau M, Maderna E, Cappella A, Caudullo G, Scarpulla V, Cattaneo C (2018) A comparative analysis of microscopic alterations in modern and ancient undecalcified and decalcified dry bones. Am J Phys Anthropol 165(2):363–369

Castro W, Hoogewerff J, Latkoczy C, Almirall JR (2010) Application of laser ablation (LA-ICP-SF-MS) for the elemental analysis of bone and teeth samples for discrimination purposes. Forensic Sci Int 195(1–3):17–27

Cattaneo C, Porta D, Gibelli D, Gamba C (2009) Histological determination of the human origin of bone fragments. J Forensic Sci 54:531–533

Cattaneo C, Mazzarelli D, Cappella A, Castoldi E, Mattia M, Poppa P, De Angelis D, Vitello A, Biehler-Gomez L (2018) A modern documented Italian identified skeletal collection of 2127 skeletons: the CAL Milano Cemetery Skeletal Collection. Forensic Sci Int 287: 219e.1–219.e5

Chadefaux C, Hô AL, Bellot-Gurlet L, Reiche I (2009a) Curve-fitting micro-ATR FTIR studies of the amide I and amide II bands of type I collagen in archaeological bone materials. E-Preservation Sci 6: 129–137

Chadefaux C, Vignaud C, Chalmin E, Robles-Camacho J, Arroyo-Cabrales J, Johnson E, Reiche I (2009b) Color origin and heat evidence of paleontological bones: case study of blue and gray bones from San Josecito Cave,Mexico. Am Mineral 94:27–33

Cheary RW, Coelho A (1992) A fundamental parameters approach to X-ray line-profile fitting. J Appl Crystallogr 25:109–121

Child AM (1995a) Towards an understanding of the microbial decomposition of archaeological bone in the burial environment. J Archaeol Sci 22:165–174

Child AM (1995b) Microbial taphonomy or archaeological bone. Stud Conserv 40:19–30

Collins MJ, Nielsen-Marsh CM, Hiller J, Smith CI, Roberts JP, Prigodich RV, Wess TJ, Csapo J, Millard AR, Turner-Walker G (2002) The survival of organic matter in bone: a review. Archaeom. 44:383–394

Cooper DML, Turinsky AL, Sensen CW, Hallgrimsson B (2003) Quantitative 3D analysis of the canal network in cortical bones by micro-computed tomography. J Archaeol Sci 274B:169–179

Dal Sasso G, Maritan L, Usai D, Angelini I, Artioli G (2015) Bone diagenesis at the micro-scale: bone alteration patterns during multiple burial phases at Al Khiday (Khartoum, Sudan) between the Early Holocene and the II century AD. Palaeogeogr Palaeoclimatol Palaeoecol 416:30–42

Dal Sasso G, Asscher Y, Angelini I, Nodari L, Gilberto A (2018) A universal curve of apatite crystallinity for the assessment of bone integrity and preservation. Sci Rep 8:12025

De Carlo F, Gürsoy D, Marone F, Rivers M, Parkinson DY, Khan F, Schwarz N, Vine DJ, Vogt S, Gleber SC, Narayanan S, Newville M, Lanzirotti T, Sun Y, Hong YP, Jacobsen C (2014) Scientific data exchange: a schema for hdf5-based storage of raw and analyzed data. J Synchrotron Radiat 21:1224–1230

Evans JA, Chenery CA, Fitzpatrick AP (2006) Bronze age childhood migration ofindividuals near stonehenge, revealed by strontium and oxygen isotope tooth enamel analysis. Archaeom. 8(2):309–321

Fernández-Jalvo Y, Andrews P, Pesquero D, Smith C, Marín-Monfort D, Sánchez B, Geigl E-M, Alonso A (2010) Early bone diagenesis in temperate environments. Palaeogeogr Palaeoclimatol Palaeoecol 288(1-4):62–81

France CAM, Thomas DB, Doney CR, Madden O (2014) FT-Raman spectroscopy as a method for screening collagen diagenesis in bone. J Archaeol Sci 42:346–355

Guarino FM, Angelini F, Vollono C, Orefice C (2006) Bone preservation in human remains from the Terme del Sarno at Pompeii using light microscopy and scanning electron microscopy. J Archaeol Sci 33(4):513–520

Hackett CJ (1981) Microscopical focal destruction (tunnels) in exhumed human bones. Med Sci Law 21(4):243–265

Han S-H, Kim S-H, Ahn Y-W, Huh G-Y, Kwak D-S, Park D-K, Lee U-Y, Kim Y-S (2009) Microscopic age estimation from the anterior cortex of the femur in Korean adults. J Forensic Sci 54:519–522

Hedges REM (2002) Bone diagenesis: an overview of processes. Archaeom. 44:319–328

Hedges REM, Millard AP, Pike AWG (1995) Measurements and relationships of diagenetic alteration of bone from three archaeological sites. J Archaeol Sci 22:201–209

Hollund HI, Jans MM, Collins MJ, Kars H, Joosten I, Kars SM (2012) What happened here? Bone histology as a tool in decoding the postmortem histories of archaeological bone from Castricum, The Netherlands. Int J Osteoarchaeol 22:537–548

Hollund HI, Aariese F, Fernandes R, Jans MME, Kars K (2013) Testing an alternative high-throughput tool for investigating bone diagenesis: FTIR in attenuated total reflection (ATR) mode. Archaeom. 55(3):507–532

Hollund HI, Blank M, Sjögren K-G (2018) Dead and buried? Variation in post-mortem histories revealed through histotaphonomic characterisation of human bone from megalithic graves in Sweden. PLoS One 13:e0204662. https://doi.org/10.1371/journal.pone.0204662

Huisman H, Ismail-Meyer K, Sageidet BM, Joosten I (2017) Micromorphological indicators for degradation processes in archaeological bone from temperate European wetland sites. J Archaeol Sci 85:13–29

Işcan YM, Loth S, Wright R (1984) Age estimation from the rib by phase analysis: white males. J Forensic Sci 29:1094–1104

Jackes M, Sherburne R, Lubell D, Barker C, Wayman M (2001) Destruction of microstructure in archaeological bone: a case study from Portugal. Int J Osteoarchaeol 11(6):415–432

Jans MM, Nielsen-Marsh C, Smith CI, Collins MJ, Kars H (2004) Characterisation of microbial attack on archaeological bone. J Archaeol Sci 31(1):87–95

Keenan SW, Engel AS, Roy A, Bovenkamp-Langlois GL (2015) Evaluating the consequences of diagenesis and fossilization on bioapatite lattice structure and composition. Chem Geol 413:18–27

Kendall C, Høier Eriksen AM, Kontopoulos I, Collins MJ, Turner-Walker G (2018) Diagenesis of archaeological bone and tooth. Palaeogeogr Palaeoclimatol Palaeoecol 491:21–37

Kerley ER, Ubelaker DH (1978) Revisions in the microscopic method of estimating age at death in human cortical bone. Am J Phys Anthropol 49:545–546

Kontopoulos I, Penkman K, Liritzis I, Collins MJ (2019) Bone diagenesis in a Mycenaean secondary burial (Kastrouli, Greece). Archaeol Anthropol Sci 11(10):5213–5230

Le Garff E, Mesli V, Delannoy Y, Colard T, De Jonckheere J, Demondion X, Hédouin V (2017a) The precision of micro-tomography in bone taphonomic experiments and the importance of registration. Forensic Sci Int 273:161–167

Le Garff E, Mesli V, Delannoy Y, Colard T, Demondion X, Becart A, Hédouin V (2017b) Early post-mortem changes of human bone in taphonomy with μCT. Int J Legal Med 131(3):761–770

Lebon M, Müller K, Bahain J, Fröhlich F, Falguères C, Bertrand L, Sandt C, Reiche I (2011) Imaging fossil bone alterations at the microscale by SR-FTIP microspectroscopy. J Anal At Spectrom 26:922–929

Lebon M, Zazzo A, Reiche I (2014) Screening in situ bone and teeth preservation by ATR-FTIR mapping. Palaeogeogr Palaeoclimatol Palaeoecol 416:110–119

Lebon M, Reiche I, Gallet X, Bellot-Gurlet L, Zazzo A (2016) Rapid quantification of bone collagen content by ATR-FTIR Spectroscopy. Radiocarbon 58:131–145

Maggiano IS, Maggiano CM, Clement JG, Thomas CD, Carter Y, Cooper DM (2016) Three-dimensional reconstruction of Haversian systems in human cortical bone using synchrotron radiation-based micro-CT: morphology and quantification of branching and transverse connections across age. J Anat 228(5):719–732

Marado LM, Braga C, Fontes L (2018) Bone diagenesis in via XVII inhumations (Bracara Augusta): identification of taphonomic and environmental factors in differential skeletal preservation. Estudos do Quaternário 18:67–76

Margariti E, Stathopoulou ET, Sanakis Y, Kotopoulou E, Pavlakis P, Godelitsas A (2019) A geochemical approach to fossilization processes in Miocene vertebrate bones from Sahabi, NE Libya. J Afr Earth Sci 149:1–18

Marques MPM, Mamede AP, Vassalo AR, Makhoul C, Cunha E, Gonçalves D, Parker SF, Batista de Carval LAE (2018) Heat-induced bone diagenesis probed by vibrational spectroscopy. Sci Rep 8:15935

Marsden I, Pagani C (2008) Milano, Viale Sabotino (MI). Indagini archeologiche. In *Notiziario 2006*, Milan.

Molin G, Salviulo G, Guerriero P (2002) A crystal-chemical study of remains found in the tomb of Giuseppe Tartini (1692-1770). Archaeom. 11(1):107–116

Monge G, Carretero MI, Pozo M, Barroso C (2014) Mineralogical changes in fossil bone from Cueva del Angel, Spain: archaeological implications and occurrence of whitlockite. J Archaeol Sci 46:6–15

Morales NS, Catella L, Oliva F, Sarmiento PL, Barrientos G (2017) A SEM-based assessment of bioerosion in Late Holocene faunal bone assemblages from the southern Pampas of Argentina. J Archaeol Sci Rep 18:782–791

Müller K, Chadefaux C, Thomas N, Reiche I (2011) Microbial attack of archaeological bones versus high concentrations of heavy metals in the burial environment. A case study of animal bones from a mediaeval copper workshop in Paris. Palaeogeogr Palaeoclimatol Palaeoecol 310(1–2):39–51

Munch B, Trtik P, Marone F, Stampanoni M (2009) Stripe and ring artifact removal with combined wavelet–Fourier filtering. Opt Express 17:8567–8591

Nielsen-Marsh CM, Hedges REM (2000) Patterns of diagenesis in bone I: the effect of site environments. J Archaeol Sci 27:1139–1150

Nielsen-Marsh CM, Smith CI, Jans MM, Nord A, Kars H, Collins MJ (2007) Bone diagenesis in the european Holocene II: taphonomic and environmental considerations. J Archaeol Sci 34(9):1523–1531

Palacio-Mancheno PE, Larriera AI, Doty SB, Cardoso L, Fritton SP (2014) 3D assessment of cortical bone porosity and tissue mineral density using high-resolution μCT: effects of resolution and threshold method. JBMR 29(1):142–150

Person A, Bocherens H, Saliège J-F, Paris F, Zeitoun V, Gérard M (1995) Early diagenetic evolution of bone phosphate: an X-ray diffractometry analysis. J Archaeol Sci 22:211–221

Peyrin F, Dong P, Pacureanu A, Langer M (2014) Micro- and nano-CT for the study of bone ultrastructure. Curr Osteoporos Rep 12:465–474

Piga G, Santos-Cubedo A, Solà SM, Brunetti A, Malgosa A, Enzo S (2009) An X-ray Diffraction (XRD) and X-ray Fluorescence (XRF) investigation in human and animal fossil bones from Holocene to Middle Triassic. J Archaeol Sci 36(9):1857–1868

Piga G, Santos-Cubedo A, Brunetti A, Piccinini M, Malgosa A, Napolitano E, Enzo S (2011) A multi-technique approach by XRD, XRF, FT-IR to characterize the diagenesis of dinosaur bones from Spain. Palaeogeogr. Palaeoclimatol Palaeoecol 310(1–2):92–107

Piga G, Solinas G, Thompson TJU, Brunetti A, Malgosa A, Enzo S (2013) Is X-ray diffraction able to distinguish between animal and human bones? J Archaeol Sci 40:778–785

Prieto-Castelló MJ, Hernández del Rincón JP, Pérez-Sirvent C, Alvarez-Jiménez P, Pérez-Cárceles MD, Osuna E, Luna A (2007) Application of biochemical and X-ray diffraction analyses to establish the postmortem interval. Forensic Sci Int 172:112–111

Reiche I, Vignaud C, Menu M (2002) The crystallinity of ancient bone and dentine: new insights by transmission electron microscopy. Archaeom. 44:447–459

Reiche I, Lebon M, Chadefaux C, Müller K, Le Hô A-S, Gensch M, Schade U (2010) Microscale imaging of the preservation state of 5,000-year-old archaeological bones by synchrotron infrared microspectroscopy. Anal Bioanal Chem 397:2491–2499

Robinson S, Nicholson RA, Pollard AM, O'Connor TP (2003) An evaluation of nitrogen porosimetry as a technique for predicting taphonomic durability in animal bone. J Archeol Sci 30:391–403

Rogoz A, Sawlowicz Z, Wojtal P (2012) Diagenetic history of woolly mammoth (mammuthus primigenius) skeletal remains from the archaeological site cracow Spadzista Street (B), Southern Poland. PALAIOS 27:541–549

Rouge-Maillart C, Vielle B, Jousset N, Chappard D, Telmon N, Cunha C (2009) Development of a method to estimate skeletal age at death in

adults using the acetabulum and the auricular surface on a Portuguese population. Forensic Sci Int 188:91–95

Ryanskaya AD, Kiseleva DV, Shilovsky OP, Shagalov ES (2019) XRD study of the Permian fossil bone tissue. Powder Diffract 34(S1): S14–S17. https://doi.org/10.1017/S0885715619000174

Sannazaro M (2001) *La necropoli tardoantica: ricerche archeologiche nei cortili dell'Università cattolica*. Vita e Pensiero, Milan, Milano

Schindelin J, Arganda-Carreras I, Frise E, Kaynig V, Longair M, Pietzsch T, Preibisch S, Rueden C, Saalfeld S, Schmid B, Tinevez JY, White DJ, Hartenstein V, Eliceiri K, Tomancak P, Cardona A (2012) Fiji: an open-source platform for biological-image analysis. Nat Methods 9(7):676–682

Schmahl WW, Kocsis B, Toncala A, Grupe G (2016) Mineralogic characterisation of archaeological bone. In: Grupe G, McGlynn G (eds) *Isotopic landscapes in bioarchaeology*. Springer, Berlin, Heidelberg

Smith CI, Faraldos M, Fernández-Jalvo Y (2008) The precision of porosity measurements: effects of sample pre-treatment on porosity measurements of modern and archaeological bone. Palaeogeogr Palaeoclimatol Palaeoecol 266:175–182

Soltan N, Kawalilak CE, Cooper DM, Kontulainen SA, Johnston JD (2019) Cortical porosity assessment in the distal radius: a comparison of HR-Pqct measures with Synchrotron-Radiation micro-CT-based measures. Bone 120:439–445

Squires KE, Thompson TJU, Islam M, Chamberlain A (2011) The application of histomorphometry and Fourier transform infrared spectroscopy to the analysis of early Anglo-Saxon burned bone. J Archaeol Sci 38:2399e2409

Stathopoulou E, Theodoropoulou T, Phoca-Cosmetatou N (2013) Black fish bones in waterlogged deposits: the case of the Neolithic lake settlement of Dispilio, Greece. Archaeofauna 22:51–74

Sudarsan K, Young RA (1969) Significant precision in crystal structural details: Holly Springs hydroxyapatite. Acta Cryst B25:1534

Szostek K, Stepańczak B, Szczepanek A, Kępa M, Głąb H, Jarosz P, Włodarczak P, Tunia K, Pawlyta J, Paluszkiewicz C, Tylko G (2011) Diagenetic signals from ancient human remains-bioarchaeological applications. Mineralogia 42(2-3):93–112

Tripp JA, Squire ME, Hedges REM, Stevens RE (2018) Use of micro-computed tomography imaging and porosity measurements as indicators of collagen preservation in archaeological bone. Palaeogeogr Palaeoclimatol Palaeoecol 511:462–471

Trueman CNG, Martill DM (2002) The long-term preservation of bone: the role of bioerosion. Archaeom. 44:371–382

Trueman CNG, Behrensmeyer AK, Tuross N, Weiner S (2004) Mineralogical and compositional changes in bones exposed on soil surfaces in Amboseli National Park, Kenya: diagenetic mechanisms and the role of sediment pore fluids. J Archaeol Sci 31:721–739

Trueman CN, Privat K, Field J (2008) Why do crystallinity values fail to predict the extent of diagenetic alteration of bone mineral? Palaeogeogr Palaeoclimatol Palaeoecol 266:160–167

Turner-Walker G (2012) Early bioerosion in skeletal tissues: persistence through deep time. Neues Jahrb Geol Palaontol Abh 265(2):165–183

Turner-Walker G, Jans MM (2008) Reconstructing taphonomic histories using histological analysis. Palaeogeogr Palaeoclimatol Palaeoecol 266:227–235

Turner-Walker G, Syversen U (2002) Quantifying histological changes in archaeological bones using BSE-SEM image analysis. Archaeom. 44:461–468

Turner-Walker G, Nielsen-Marsh CM, Syversen U, Kars H, Collins MJ (2002) Sub-micron spongiform porosity is the major ultra-structural alteration occurring in archaeological bone. Int J Osteoarchaeol 12: 407–414

Wei M, Ruys AJ, Milthorpe BK, Sorrell CC (1999) Solution ripening of hydroxyapatite nanoparticles: effects on electrophoretic deposition. J Biomed Mater Res 45(1):11–19

Weiner S, Wagner HD (1998) The material bone: structure-mechanical function relations. Annu Rev Mater Sci 28:271–298

White L, Booth TJ (2014) The origin of bacteria responsible for bioerosion to the internal bone microstructure: results from experimentally-deposited pig carcasses. Forensic Sci Int 239:92–102

Wilson LYN, Pollard AM (2002) Here today, gone tomorrow? Integrated experimentation and geochemical modeling in studies of archaeological diagenetic change. Acc Chem Res 35:644–651

Winer S, Bar-Yosef O (1990) States of preservation of bones from prehistoric sites in the Near East: a survey. J Archaeol Sci 17(2):187–196

Wopenka B, Pasteris JD (2005) A mineralogical perspective on the apatite in bone. Mater Sci Eng C 25(2):131–143

Young RA (1993) *The Rietveld method*, Oxford University Press.